Dual-season and full-polarimetric C band SAR assessment for vegetation mapping in the Amazon *várzea* wetlands

Luiz Felipe de Almeida Furtado [a,*], Thiago Sanna Freire Silva [b], Evlyn Márcia Leão de Moraes Novo [a]

[a] *Divisão de Sensoriamento Remoto, Instituto Nacional de Pesquisas Espaciais (INPE), Avenida dos Astronautas 1758, Jardim da Granja, São José dos Campos, SP 12227-010, Brazil*
[b] *Instituto de Geociências e Ciências Exatas, UNESP — Univ. Estadual Paulista, Departamento de Geografia, Ecosystem Dynamics Observatory, Avenida 24A, 1515, Rio Claro, SP 13506-900, Brazil*

ARTICLE INFO

ABSTRACT

This study answered the following questions: 1) Is polarimetric C-band SAR (PolSAR) more efficient than dual-polarization (dual-pol) C-band SAR for mapping *várzea* floodplain vegetation types, when using images of a single hydrological period? 2) Are single-season C-band PolSAR images more accurate for mapping *várzea* vegetation types than dual-season dual-pol C-band SAR images? 3) What are the most efficient polarimetric descriptors for mapping *várzea* vegetation types? We applied the Random Forests algorithm to classify dual-pol SAR images and polarimetric descriptors derived from two full-polarimetric Radarsat-2 C-band images acquired during the low and high water seasons of Lago Grande de Curuai floodplain, lower Amazon, Brazil. We used the *Kappa* index of agreement (κ), *Allocation Disagreement* (AD) and *Quantity Disagreement* (QD), and Producer's and User's accuracy measurements to assess the classification results. Our results showed that single-season full-polarimetric C-band data can yield more accurate classifications than single-season dual-pol C-band SAR imagery and similar accuracies to dual-season dual-pol C-band SAR classifications. Still, dual-season PolSAR achieved the highest accuracies, showing that seasonality is paramount for obtaining high accuracies in wetland land cover classification, regardless of SAR image type. On average, single-season classifications of low-water periods were less accurate than high-water classifications, likely due to plant phenology and flooding conditions. Classifications using model-based polarimetric decompositions (such as Freeman–Durden, Yamaguchi and van Zyl) produced the highest accuracies (κ greater than 0.8; AD ranging from 7.5% to 2.5%; QD ranging from 15% to 12%), while eigenvector-based decompositions such as Touzi and Cloude–Pottier had the worst accuracies (κ ranging from 0.5 to 0.7; AD greater than 10%; QD smaller than 10%). Vegetation types with dense canopies (Shrubs, Floodable Forests and Emergent Macrophytes), whose classification is challenging using C-band, were accurately classified using dual-season full-polarimetric SAR data, with Producer's and User's accuracies between 80% and 90%. We conclude that full polarimetric C-band imagery can yield very accurate classifications of *várzea* vegetation (κ ~0.8, AD ~3% and QD ~10%) and can be used as an operational tool for forested wetland mapping.

1. Introduction

Várzeas are Amazon wetland ecosystems located on sediment-rich ("white water") river floodplains (Junk, 1997), covering 12% to 29% of the Amazon River basin (Melack & Hess, 2010). *Várzea* vegetation types can be classified based on different criteria; Junk, Piedade, Schöngart, and Wittmann (2012) provide a comprehensive, hierarchical classification that initially divides *várzea* vegetation into two categories: Systems predominantly covered with (1) herbaceous plants or (2) woody plants. The first group is subdivided into three subgroups according to phenology, species composition and terrain elevation: (a) Low-lying areas mostly covered by annual grasses and herbs, (b) Low-lying areas mostly covered by perennial grasses and (c) High-

lying disturbed areas with annual and perennial grasses and herbs. The second group is subdivided according to flood duration: (a) Low *várzea* forests (>3 months of flooding per year); (b) High *várzea* forests (<3 months of flooding per year) and (c) Swamp forests (which may have permanent or multiannual flooding periods). Human-induced land cover changes often modify the expected spatial distribution of these plant communities, affecting the observed proportions between vegetation types (Junk et al., 2012; Junk, Bayley & Sparks, 1989; Renó, Novo, Almeida-Filho and Suemitsu, 2011a; Renó, Novo, Suemitsu, Rennó and Silva, 2011b; Wittmann, Schöngart, & Junk, 2010; Wittmann, Junk, & Piedade, 2004).

Várzeas provide several ecosystem services that are important for the survival and quality of life of riverine human populations, such as water consumption, runoff reduction and slope stabilization, wood and forest products, and fisheries. *Várzea* ecosystems also host a wide range of distinctive fauna and flora, including the Amazonian manatee (*Trichechus*

* Corresponding author.
  E-mail address: furtadosere@gmail.com (L.F.A. Furtado).

inunguis) (Arraut et al., 2010) and the *pirarucu* fish (*Arapaima gigas*) (Arantes, Castello, Cetra, & Schilling, 2013), and have an important role in regional biogeochemical cycles, functioning as both sinks and sources of greenhouse gases (CO_2 and CH_4). Despite its importance, *várzea* wetlands have been increasingly threatened by anthropogenic land use/ land cover change and economic appropriation of the space for agriculture, pastures and commercial fishery activities (Castello et al., 2013). About 54% of the forest cover in the lower Amazon River *várzea* has been removed or replaced by other vegetation types and/or land uses between 1970 and 2008 (Renó et al., 2011a; Renó et al., 2011b).

Radar remote sensing has been an important tool for monitoring *várzea* ecosystems, especially given their extent and complexity. Synthetic Aperture Radar (SAR) microwaves can penetrate clouds, common in tropical and equatorial latitudes, and interact three-dimensionally with the vegetation, detecting both canopy structural characteristics and the flooding beneath it. SAR applications in *várzea* began in the 1980s with the *Shuttle Imaging Radar* (SIR-A, -B and -C) and other airborne missions (Hess, Melack, & Simonett, 1990; Kasischke, Melack, & Dobson, 1997), and progressed with several satellite systems such as ERS-1 and ERS-2 (C-band), JERS-1 and ALOS/PALSAR (L-band) and Radarsat (C-band) (Silva, Melack, Streher, Ferreira-Ferreira, & de A. Furtado, 2015; Henderson & Lewis, 2008), including the only comprehensive wetlands mapping for the entire Amazon Basin (Hess et al., 2015; Hess, Melack, Novo, Barbosa, & Gastil, 2003; Melack & Hess, 2010).

Most past platforms have only been capable of *single-* or *dual-polarization* (dual-pol) configurations, with limited potential for discriminating *várzea* vegetation types with subtle structural differences (Silva, Costa, & Melack, 2010; Hess et al., 1990). Dual or multi-seasonal imagery (Hess et al., 2003; Martinez & Le Toan, 2007; Silva et al., 2010) multiple incidence angles (Lang, Townsend, & Kasischke, 2008; Marti-Cardona, Lopez-Martinez, Dolz-Ripolles, & Bladè-Castellet, 2010) and/or multiple wavelengths (Costa, 2004; Costa, Niemann, Novo, & Ahern, 2002; Hess et al., 1995) have all been explored to overcome such limitations, with the dual or multi-season approach offering the best balance between feasibility and effectiveness (Silva et al., 2015).

Modern spaceborne platforms such as TerraSAR-X (X band), Radarsat-2 (C band) and ALOS-PALSAR-2 (L band) have *full polarimetric* or *quad-pol* imaging modes (PolSAR), as did a few previous platforms such as SIR-C (multi-frequency) and ALOS/PALSAR (L-band). Full polarimetric systems allow the reconstruction of the complete scattering matrix of the backscattered wave, permitting the calculation of polarimetric decompositions and other polarimetric descriptors (Lee & Pottier, 2009) to quantify the contribution of different scattering mechanisms to the resulting backscattered signal. Several studies have highlighted the potential of PolSAR imagery for wetlands research (Brisco et al., 2013; Brisco, Kapfer, Hirose, Tedford, & Liu, 2011; Gosselin, Touzi and Cavayas, 2013), but some questions remain underexplored in wetlands research, especially in *várzea* regions.

Therefore, we used two full-polarimetric C-band Radarsat-2 images acquired in two different periods of the hydrological year to answer the following questions: 1) Is polarimetric C-band SAR (PolSAR) more efficient than dual-polarization (dual-pol) C-band SAR for mapping *várzea* floodplain vegetation types, when using images of a single hydrological period? 2) Are single-season C-band PolSAR images more accurate for mapping *várzea* vegetation types than dual-season dual-pol C-band SAR images? 3) What are the most efficient polarimetric descriptors for mapping *várzea* vegetation types?

2. Methods

2.1. Study area

Lago Grande de Curuai (Fig. 1) is a large floodplain lake complex located to the south of the city of Óbidos (Pará, Brazil). The Curuai floodplain has an annual and monomodal flooding regime, with peak flooding (high water season) occurring between May and June, and minimal flooding (low water season) occurring between November and December. Annual differences in water stage height between the two periods vary between 5 and 7 m at the deepest parts of the lake (Rudorff, Melack, & Bates, 2014).

2.2. Data acquisition and processing

We used two full-polarimetric Radarsat-2 (RS2) images (C band, ~5.6 cm wavelength) acquired in 2011–06–22 (high water season — HW) and 2011–10–20 (low water season — LW), with approximately 8×5 m (range × azimuth) spatial resolution and 25° (SQ7) incidence angle. Other incidence angles (35° − SQ14 and 45° − SQ27) were assessed, but did not have significant effects on mapping accuracy. Furthermore, previous research recommends steep incidence angles for wetland/*várzea* mapping applications (Hess et al., 1990; Silva et al., 2008).

PolSAR processing consisted of (Fig. 2): (1) *multilooking* with 4 looks in azimuth and 1 in range, resulting in approximately 20×20 m ground-range spatial resolution; (2) covariance (C) and coherence (T) matrix calculation; (3) speckle noise filtering using the *Refined Lee* adaptive filter with a 5×5 mask; (4) calculation of polarimetric decompositions (Table 1); (5) sigma-nought (σ^0) calibration; and (6) Range–Doppler terrain correction and georeferencing. To preserve both spatial resolution and edges between surface targets, we did not use spatial averaging kernels to calculate polarimetric decompositions. Speckle was already mitigated by both multilooking and the use of speckle filtering.

We applied Range–Doppler terrain correction using the Shuttle Radar Topography Mission (SRTM) digital elevation model (DEM) (Jarvis, Reuter, & Nelson, 2008). This DEM has 90 m spatial resolution and approximately 5 m vertical resolution (Bhang, Schwartz, & Braun, 2007), and it was obtained at http://srtm.csi.cgiar.org/at its version 4.

We georeferenced the RS2 images using a Landsat5/TM *Global Land Survey 2000* (USGS, 2009) image, obtained at http://glcf.umd.edu/data/landsat/. Polarimetric decompositions were performed using the *Polarimetric SAR Data Processing and Educational Tool* (PolSARPRO) software, version 4.2 (Pottier et al., 2009), which was also used for multilooking, speckle filtering and σ^0 calibration, the latter using image metadata, with ± 1 dB expected radiometric error. We performed Range–Doppler terrain correction using the Next ESA SAR Toolbox (NEST), version 4C-1.1 (Engdahl, Minchella, Marinkovic, Veci, & Lu, 2012).

2.3. Image classification

We grouped backscattering and polarimetric decomposition attributes into 27 different sets to serve as inputs for classification, based on the nature of the data and seasonality (high water, low water or dual-season, Table 2). It was thus possible to compare and assess classification accuracies between (a) single- and dual-season classifications, (b) dual-pol SAR (HH + HV) and PolSAR data, and (c) among different polarimetric attributes.

Prior to classification, we segmented all images using the multiresolution segmentation algorithm implemented in eCognition 8.0, with the parameters *Scale* = 8, *Shape* = 0.1 and *Compactness* = 0.5. We defined these parameters based (a) on previous studies (Furtado, Silva, Fernandes, & Novo, 2015) and (b) trial and error/heuristic approach. The selected parameters gave more importance to image radiometry (*Shape* = 0.1) and balanced natural and human-made target contours (*Compactness* = 0.5). *Scale* values between 5 and 50 were tested, and the value of 8 was selected as optimal, based on the visual interpretation of segmentation results (Fig. 3).

We created a single segmentation layer using dual-season C matrix main diagonal images as inputs (corresponding to HH, HV and VV polarizations) and used it for all classifications. The C matrix diagonal contains most of the scattering matrix information, has a higher signal-to-noise ratio than other polarimetric descriptors, and has better edge
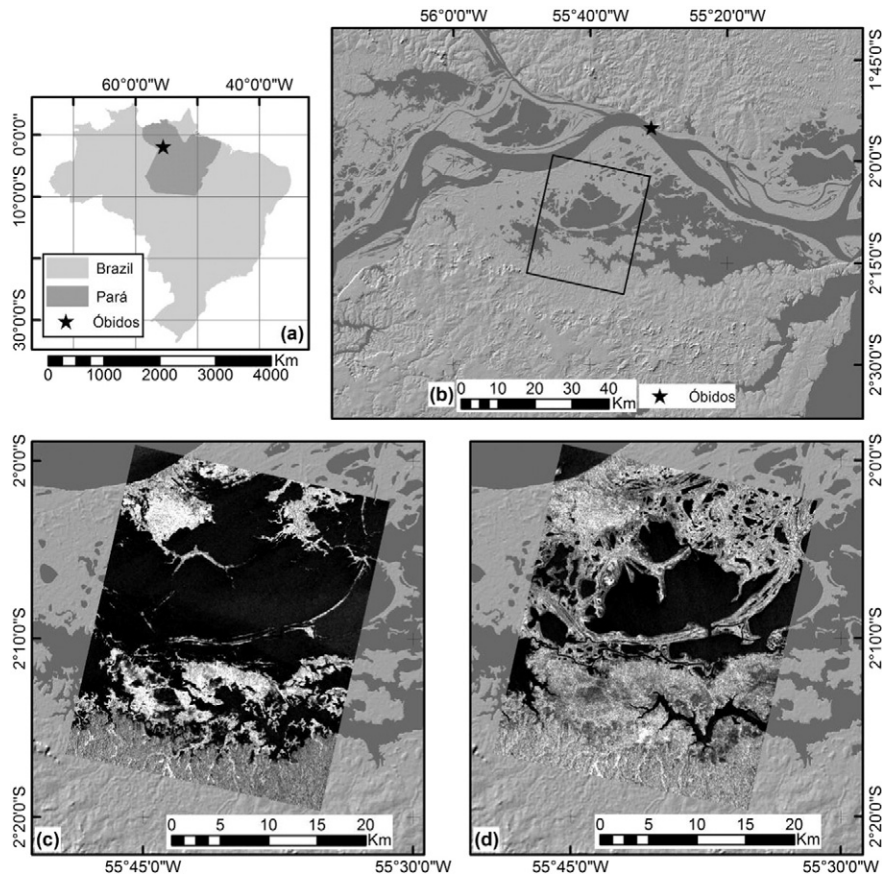
Fig. 1. (a) Location of Pará state (dark gray) within Brazil (light gray), showing the location of Óbidos municipality (black star); (b) detailed view of the Lago Grande de Curuai floodplain water surfaces (dark gray), highlighting the Radarsat-2 (RS2) image coverage (black polygon). At the bottom, detailed view of (c) high water season and (d) low water season Radarsat-2 HH images extracted from POLSAR datasets. Radarsat-2 products are licensed for use by MacDonald, Dettwiler and Associates, Ltd.
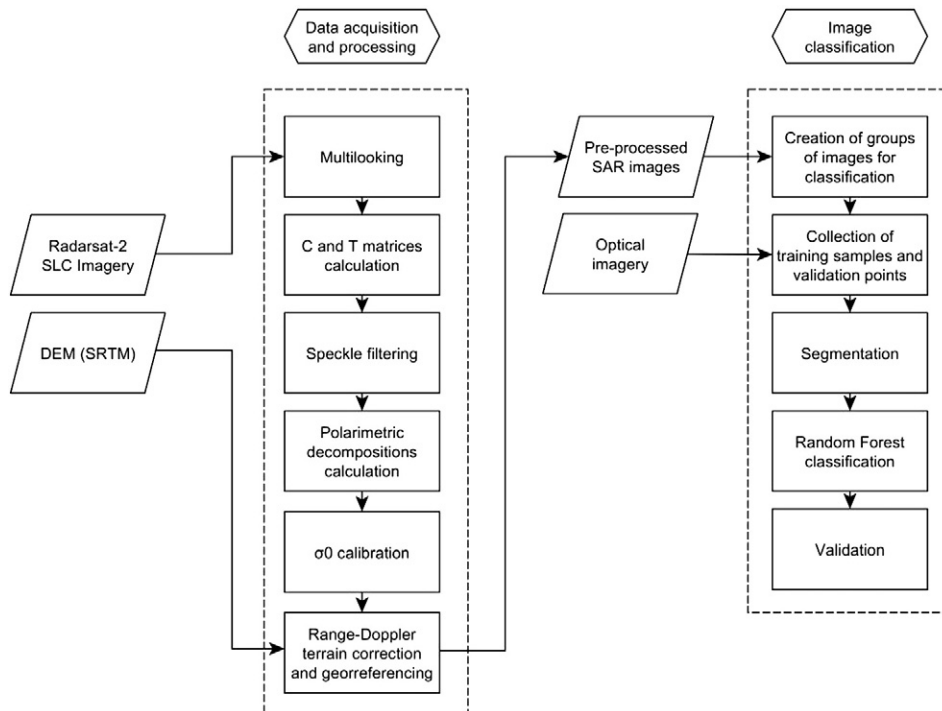

Fig. 2. Data acquisition, image processing and image classification workflow for classifying vegetation types land cover in the Lago Grande de Curuai *várzea* (Amazon, Brazil) using Radarsat-2 full polarimetric images.

Table 1

Polarimetric decompositions extracted from dual-season Radarsat-2 PolSAR images for classifying vegetation types and land cover in the Lago Grande de Curuai *várzea* floodplain, Amazon, Brazil.

Polarimetric decomposition	Symbol	Description
Cloude–Pottier (Cloude & Pottier, 1996)		
α angle	α	Dominant scattering type
Entropy	H	Proportional importance of the dominant scattering type
Anisotropy	A	Proportional importance of secondary and tertiary scattering types
Freeman–Durden (Freeman & Durden, 1998)		
Volumetric scattering	FD_V	Proportion of volumetric scattering
Double-bounce scattering	FD_D	Proportion of double-bounce scattering
Odd scattering	FD_S	Proportion of odd (surface) scattering
Touzi (Touzi, 2007)		
Scattering type magnitude	$\alpha_{S1}; \alpha_{S2}; \alpha_{S3}; \alpha_{Sm;}$	Angle of the symmetric scattering vector direction in the trihedral–dihedral basis. Similar to Cloude–Pottier's α angle
Scattering type phase difference	$\Phi_{\alpha S1}, \Phi_{\alpha S2}, \Phi_{\alpha S3}, \Phi_{\alpha Sm}$	Phase difference between trihedral and dihedral scattering
Helicity	$\tau_1; \tau_2; \tau_3; \tau_m$	Symmetric nature of target scattering. If $\tau = 0$, target is isotropic
Orientation angle	$\psi_1; \psi_2; \psi_3; \psi_m$	Target tilt angle
Yamaguchi (Yamaguchi, Yajima, & Yamada, 2006)		
Volumetric scattering	Y_V	Proportion of volumetric scattering
Double-bounce scattering	Y_D	Proportion of double-bounce scattering
Odd scattering	Y_S	Proportion of odd (surface) scattering
Helicity	Y_H	Proportion of helix-type scattering
Van Zyl (Vanzyl 1992)		
Volumetric scattering	VZ_V	Proportion of volumetric scattering
Double-bounce scattering	VZ_D	Proportion of double-bounce scattering
Odd scattering	VZ_S	Proportion of odd (surface) scattering

detection characteristics (Qi, Yeh, Li, & Lin, 2012) (Fig. 3). After segmentation, we calculated the mean pixel value for all polarimetric descriptors in each image object and used it to compose the classification input sets.

We used the Random Forests (RF) algorithm (Breiman, 2001) to perform data classification, as implemented in the *randomForest* package (Liaw & Wiener, 2002) of the R statistical software, version 3.1.1 (R Core Team, 2014). RF is a hierarchical classification algorithm that uses n random decision trees to form a "random forest" that will classify the data based on the consensus among all trees. The RF classification procedure consists of: (1) defining a number n_{trees} of random trees; (2) randomly selecting m_{try} attributes for assessment at each individual tree node, and identifying the attribute that produces the purest leaves (i.e., the polarimetric descriptor that best discriminates the selected classes) within m_{try}; (3) building a single decision tree where all classes are discriminated in different nodes; (4) repeating this process n_{tree} times, (5) building a consensus tree based on the most selected attributes, and (6) using this consensus tree to classify the input data.

The RF algorithm is (1) less susceptible to noisy data, (2) non-parametric, and thus supports data with varying statistical distributions (such as SAR intensities, phase and polarimetric attribute images), and (3) has only two settable parameters, reducing the subjectivity factor when comparing classification accuracies among different datasets (Barrett, Nitze, Green, and Cawkwell, 2014). Still, we assessed the impact of changes in n_{trees} and m_{try} on classification accuracy, and settled

Table 2

Input sets for classification of vegetation types and land cover in the Lago Grande de Curuai *várzea* floodplain, Amazon, Brazil. Each set was separately assessed for low-water, high-water, and dual-season conditions, totaling 27 input sets.

Abbreviation	Inputs for classification
HH + HV	HH + HV (dual-pol)
C	C Matrix (including phase information)
CP	Cloude–Pottier
TZ	Touzi
VZ	Van Zyl
YG	Yamaguchi
FD	Freeman–Durden
APD	All polarimetric decompositions
APC	All images

on optimum values for each parameter by taking those that achieved the highest accuracies.

We assessed the parameter m_{try} for the following values (using $n_{trees} = 5000$): (a) one polarimetric attribute; (b) one third of the total number of polarimetric attributes; (c) the squared root of the total number of polarimetric attributes; (d) half of the total number of polarimetric attributes, (e) two thirds of the total number of polarimetric attributes; (f) all polarimetric attributes. After selecting the best m_{try} value, we assessed the n_{trees} parameter using the following values: (a′) 250; (b′) 500; (c′) 1000; (d′) 5000; (e′) 25,000 and (f′) 50,000. Each parameter was assessed taking into account the hydrological period and the total number of images used as input.

Changes in m_{try} and n_{trees} had little or no influence on classification accuracy, using either reduced (HH + HV) or increased numbers of inputs (C matrix and APC), with a maximum difference of 0.01 in κ observed among all parameter combinations. Therefore, we set m_{try} as the squared-root of the total number of inputs, as suggested by Breiman (2001), and n_{trees} as 5000, based on previous SAR studies (Ferreira-Ferreira, Silva, Streher, Affonso, Furtado, Forsberg, & Novo, 2014).

2.4. Vegetation and land cover classes

We defined six land-cover classes for this study (Table 3), described as follows: 1) *Floodable forests* (FF): Tree vegetation growing on higher floodplain areas and subject to shorter seasonal flooding periods; 2) *shrubs* (SB): Shrubs and/or early succession arboreal vegetation with sparse canopies and low height, subject to longer seasonal flooding; 3) *emergent macrophytes* (EM): Herbaceous plant communities dominated by palustrine grasses with high biomass and density levels, and subject to longer seasonal flooding periods; 4) *floating macrophytes* (FM): Free-floating herbaceous vegetation with lower biomass and/or sparse canopies; 5) *open water* (OW): Free water surfaces; and 6) *várzea fields* (VF): Floodplain areas that are completely under water during the high water season but emerge in the low water season, being colonized by terrestrial herbaceous plants.

Since most *várzea* locations are extremely hard to reach, we defined training and validation samples based on the interpretation of several ancillary data and our extensive knowledge of the location (Table 3 and Fig. 4). Our main sources of information were geotagged photographs and field notes acquired between 2013–10–18 and 2013–10–
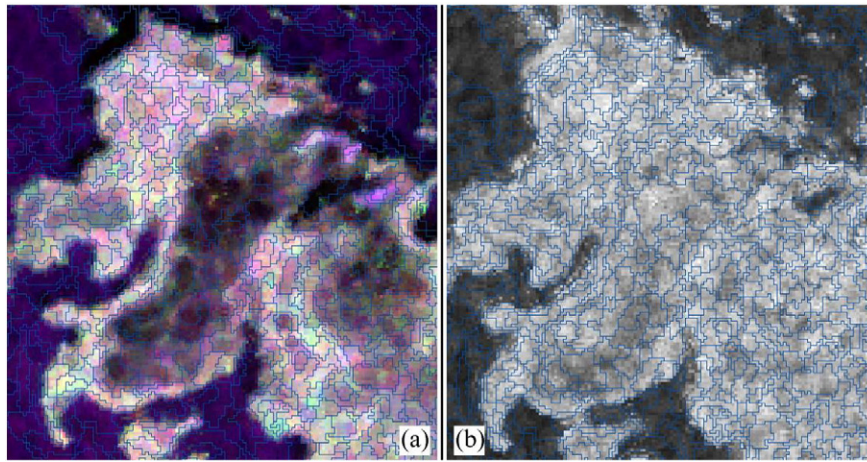
Fig. 3. Segmentation layer created using eCognition 8.0 multiresolution algorithm with Scale = 8, Shape = 0.1 and Compactness = 0.5. The edges between targets are clearly visible in (a), showing a R(HH)G(HV)B(VV) high-water season composite, while much harder to detect in (b), showing the Cloude–Pottier α angle for the high water season. Radarsat-2 products are licensed for use by MacDonald, Dettwiler and Associates, Ltd. A color version of this figure is available in the online version of this article, and the figure is presented in full-resolution in the Electronic Supplementary Material.

29, and during a previous field trip from 2011–04–10 to 2011–04–15 (Arnesen et al., 2013). These data were complemented by Google Earth™ and Microsoft Bing™ online high-resolution imagery and by Landsat5/TM scenes acquired during the same hydrological periods as the RS2 images (high-water: 2011–06–23 and 2011–07–25; low-water: 2011–10–29). Despite the two year difference between imagery and field data acquisition, all georeferenced field descriptions and photographs obtained in 2013 matched the previous land cover and vegetation types observed on Landsat5/TM and RS2 images.

2.5. Accuracy assessment

We assessed overall classification accuracy using 292 ground truth samples (Fig. 4), and the Kappa (κ) (Congalton, 1991), Quantity Disagreement (QD), and Allocation Disagreement (AD) (Pontius & Millones, 2011) accuracy indexes. We also assessed class-based accuracy, using User's and Producer's percent accuracies (Congalton, 1991). Validation samples were selected using the same criteria described above for training samples.

Table 3
Lago Grande de Curuai field photographs and image interpretation key for high and low water Radarsat-2 (R:HH, G:HV and B:VV) and Landsat5/TM (R:4, G:5, B:3) data, as well the number of selected training (T) and *validation* (V) samples. Class acronyms are: FF — floodable forests, SB — shrubs, EM — emergent macrophytes, FM — floating macrophytes, VF — *várzea* fields and OW — open water. Radarsat-2 products are licensed for use by MacDonald, Dettwiler and Associates, Ltd. A color version of this figure is available in the digital version of this article.

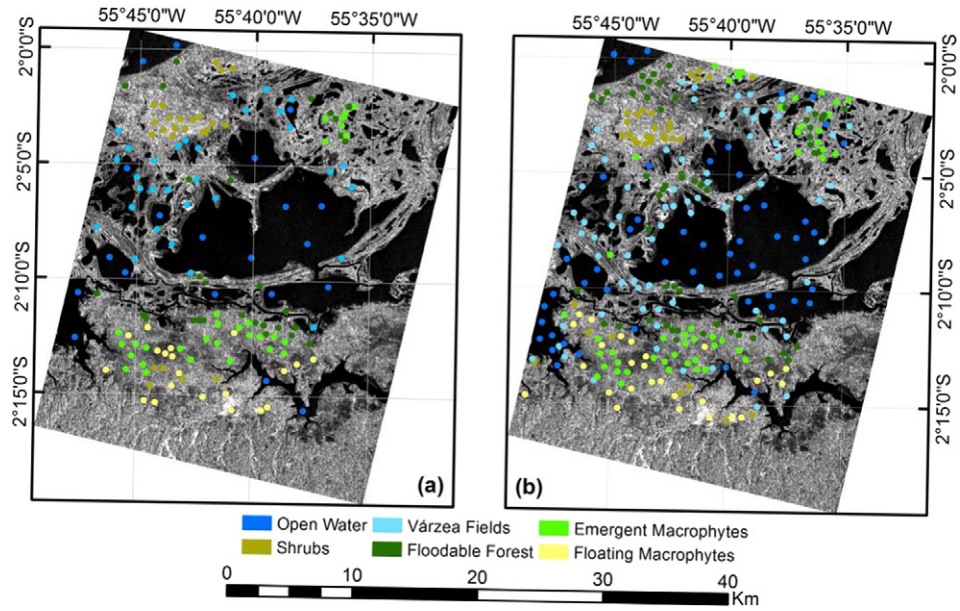| Class	Field photographs	RS2 examples	Landsat5/TM examples	#T	#V
FF				41	57
SB				33	32
EM				37	49
FM				23	30
OW				21	49
VF				36	75
TOTAL				191	292

Fig. 4. Location and spatial distribution of (a) training samples and (b) validation samples shown over a low-water RS2 HH image of Lago Grande de Curuai floodplain, Amazon, Brazil. Radarsat-2 products are licensed for use by MacDonald, Dettwiler and Associates, Ltd. A color version of this image is available in the online version of this article, and a full-resolution version is included in the Electronic Supplementary Material.
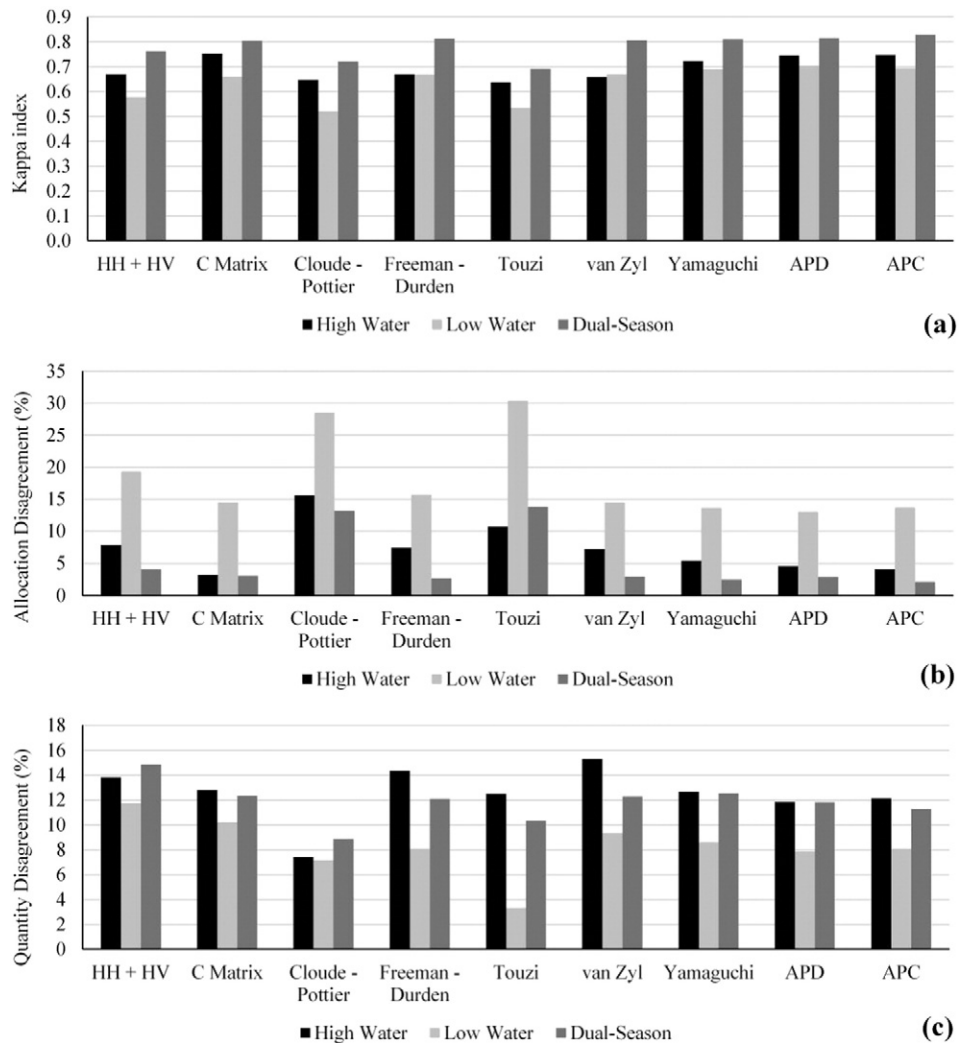

Fig. 5. Kappa (a), allocation disagreement (b) and quantity disagreement (c) for high water (blue), low water (red), and dual-season (green) várzea land cover and vegetation classification in the Lago Grande de Curuai floodplain, Amazon, Brazil.

Initially, 400 validation points were randomly created using ArcGIS 10.3, and only points with unambiguous interpretation were kept (292), ensuring that (a) every class had at least 30 validation points (Table 3) and (b) there was no spatial clustering, to avoid a positive bias. To assess the accuracy of each individual land-cover class, we compared the best and worst classification results obtained from all input sets, for a total of six classifications: two for each hydrological period (high and low-water) and two for dual-season classification. This analysis aimed to understand the interaction between polarimetric attributes and hydrological conditions when classifying each vegetation/land cover type.

3. Results

3.1. Polarimetric attribute classification accuracy

For the HW season, C matrix was the most accurate PolSAR input ($\kappa = 0.75$; AD = 3.21%; QD = 12.78%), followed by APC ($\kappa = 0.75$; AD = 4.07%; QD = 12.13%), APD ($\kappa = 0.75$; AD = 4.54%; QD = 11.84%), and the model-based decompositions of Yamaguchi ($\kappa = 0.72$; AD = 5.42%; QD = 12.67%) and Freeman–Durden ($\kappa = 0.67$; AD = 7.42%; QD = 14.35%). The classification based on the Touzi decomposition had the lowest accuracy ($\kappa = 0.64$, AD = 10.7%, QD = 12.5% (Fig. 5a, b and c, Fig. 6a and b).

On average, LW classifications were less accurate than HW, with the highest accuracy achieved by APD ($\kappa = 0.70$, AD = 13.03%, QD = 7.86%) and the lowest accuracy by the Cloude–Pottier decomposition ($\kappa = 0.52$, AD = 28.53%, QD = 7.17%). Although QD values were smaller for all LW classifications, they were disregarded as large AD errors can artificially decrease QD (Pontius & Millones, 2011). Differences between the most and least accurate classifications were smaller for the LW season than for the HW season ($\kappa = 0.66$ to 0.70; AD = 15.7% to 13%; QD = 11.73% to 8.1%).

3.2. Single-season vs. dual-season classification

Dual-season classifications were systematically more accurate than single-season classifications. Almost all dual-season classifications had higher accuracies when compared to their single-season counterparts ($\kappa = 0.75$ or higher; AD = 4% or lower; QD ranging from 11% to 15%), except for the Touzi ($\kappa = 0.69$, AD = 13.79%, QD = 10.34%) and

Cloude–Pottier ($\kappa = 0.72$, AD = 13.17%, QD = 8.86%) decompositions. The highest overall accuracy, considering all datasets, was achieved by the Dual Season APC dataset, i.e. all polarimetric decompositions plus C matrix images ($\kappa = 0.83$, AD = 2.14%, QD = 11.28%).

3.2.1. Class-specific error assessment

The use of dual-season imagery and/or the combination of several different polarimetric attributes brought the largest improvements in all class-specific accuracies (Fig. 7). In average, vegetation classes (SH, EM and FF) had a 30% to 40% increase in Producer's Accuracy and User's Accuracy when dual-season images and/or several different polarimetric descriptors (APC and APD classifications) were used. EM Producer's Accuracy increased from 46.4% to 89.2% and User's Accuracy increased from 26.5% to 67.3% between HW TZ and dual-season APD, respectively. For the SH class, Producer's Accuracy increased from 38.1% to 75% and User's Accuracy from 48.5% to 72.7% between HW TZ and dual-season APD, respectively. For the FF class, Producer's Accuracy increased from 48.6% to 79.1% and User's Accuracy increased from 64.3% to 94.6% between LW TZ and dual-season APD, respectively. Tables 4, 5 and 6 show the confusion matrices for the three most accurate classifications and Tables 7, 8 and 9 for the three least accurate classifications (all confusion matrices are available in the Electronic Supplementary Material).

4. Discussion

4.1. PolSAR responses to vegetation dynamics

Overall, our results confirm that PolSAR images are more efficient than dual-pol SAR images in mapping wetland land cover and vegetation types. PolSAR classification accuracies reported in the literature vary from 64% (Brisco et al., 2011) to 95% (Brisco et al., 2013), but more frequently between 75% and 90% (Ainsworth, Kelly, & Lee, 2009; Garcia, Roberto, Mura, Johann, & Kux, 2012; Lee, Grunes, & Pottier, 2001; Millard & Richardson, 2013; Qi et al., 2012; Sartori, Imai, Mura, Novo, & Silva, 2011). The accuracies yielded in this study ranged from $\kappa \sim 0.5$ to 0.83, AD from ~30% to 2% and QD from 15.3% to 3.33%. We consider the combination of the Random Forests algorithm and PolSAR imagery to be very effective for mapping *várzea* vegetation types, even when using shortwave C-band images, which are known to be saturated by *várzea* vegetation types with dense canopies, similar structures, and
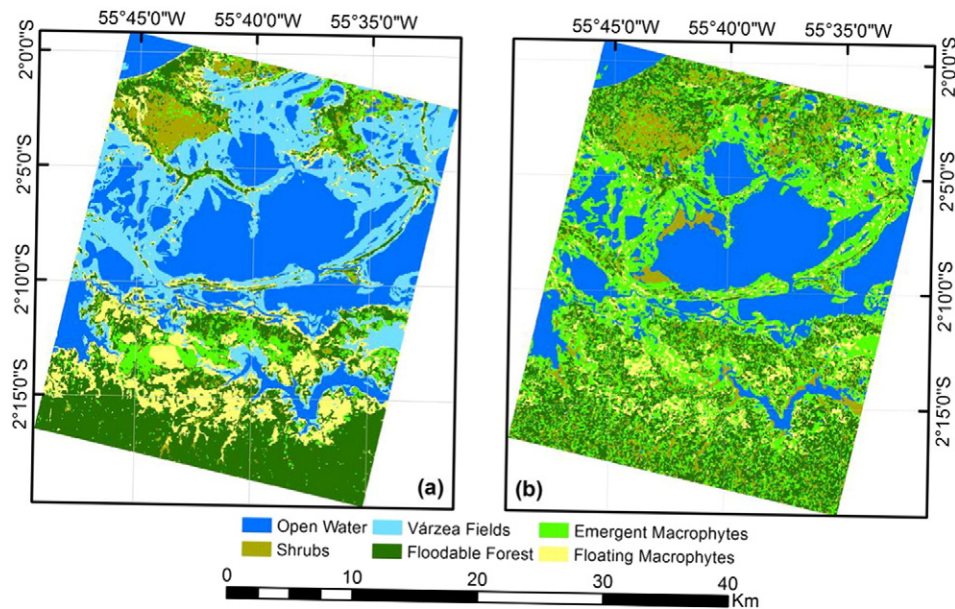

Fig. 6. Dual-season APC (a) and low-water Cloude–Pottier (b) classifications, respectively the most and least accurate *várzea* land cover and vegetation type classifications for the Lago Grande de Curuai floodplain (Amazon, Brazil). A color version of this figure is available in the online version of this article, and a full-resolution figure in presented in the Electronic Supplementary Material.
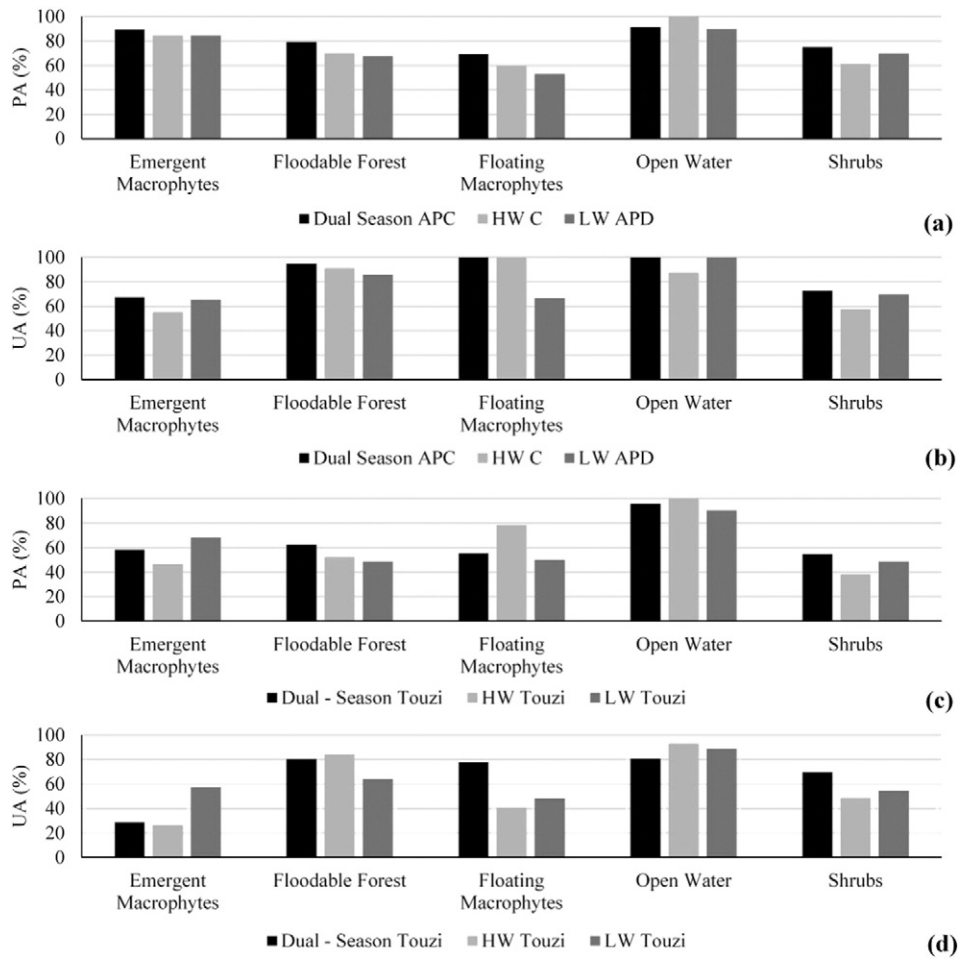
Fig. 7. Producer's Accuracy (PA) and User's Accuracy (UA) from the three most accurate – (a) and (b), respectively – and the three least accurate – (c) and (d), respectively – classifications of land cover and vegetation type in the Lago Grande de Curuai floodplain (Amazon, Brazil), expressed as percent of validation samples (n = 292). We omitted the "*Várzea* Fields" class for comparison purposes as it is present only in dual-season classifications. Confusion matrices for all evaluated classifications are available in the Electronic Supplementary Material.

similar backscattering mechanisms. Based on the results of this study, we can affirm that SAR and PolSAR images are a major source of information for *várzea* and wetland vegetation mapping, rather than a less-efficient alternative to optical imagery that should be used only when the latter is not available.

The polarimetric descriptors based on the decomposition of the T matrix eigenvectors (e.g. Touzi and Cloude–Pottier) systematically yielded lower mapping accuracies than decompositions based on scattering models (e.g. Freeman–Durden and Yamaguchi). While the van Zyl polarimetric decomposition is an eigenvector-based decomposition (van Zyl, 1992), its descriptors are similar to those generated from scattering models based on polarimetric decompositions (double-bounce,

odd and volumetric scattering), and thereby we considered van Zyl as a model-based decomposition.

Model-based polarimetric decompositions lie on the real domain and estimate the intensity of each scattering mechanism occurring in a natural target (double-bounce, volumetric and odd-scattering). These polarimetric decompositions create one individual and independent descriptor for each backscattering mechanism, better describing class scattering patterns and yielding better accuracy indexes (Brisco et al., 2011; Van Beijma, Comber, & Lamb, 2014).

Polarimetric decompositions based on eigenvector decomposition estimate target scattering mechanisms as both real and angular values. Despite the greater number of descriptors, they usually estimate the main backscattering mechanism of vegetation using a single or few components (such as Cloude–Pottier and Touzi α angles) and complement this

Table 4

Confusion matrix for dual-season all polarimetric decomposition plus C-Matrix (APC) classification, dual-season most accurate classification of Lago Grande de Curuai floodplain *várzea*. Land cover and vegetation classes are: EM — emergent macrophytes; FF — floodable forest; FM — floating macrophytes; OW — open water, SH — shrubs and VF — *várzea* fields.

Dual-season APC						
Classes	EM	FF	FM	OW	SH	VF	Total
EM	**33**	0	0	0	4	0	37
FF	9	**53**	0	0	5	0	67
FM	1	1	**27**	0	0	10	39
OW	0	0	0	**52**	0	5	57
SH	6	2	0	0	**24**	0	32
VF	0	0	0	0	0	**60**	60
Total	49	56	27	52	33	75	**292**

Table 5

Confusion matrix for high water C matrix classification, high water season most accurate classification of Lago Grande de Curuai floodplain *várzea*. Land cover and vegetation classes are: EM — emergent macrophytes; FF — floodable forest; FM — floating macrophytes; OW — open water and SH — shrubs.

High water C matrix					
Classes	EM	FF	FM	OW	SH	Total
EM	**27**	2	0	0	3	32
FF	11	**51**	0	0	11	73
FM	1	1	**27**	16	0	45
OW	0	0	0	**111**	0	111
SH	10	2	0	0	**19**	31
Total	49	56	27	127	33	**292**

Table 6

Confusion matrix for low water all polarimetric decomposition (APD) classification, low water season most accurate classification of Lago Grande de Curuai floodplain *várzea*. Land cover and vegetation classes are: EM — emergent macrophytes; FF — floodable forest; FM — floating macrophytes; OW — open water and SH — shrubs.

Low water APD						
Classes	EM	FF	FM	OW	SH	Total
EM	**81**	3	9	0	3	96
FF	17	**48**	0	0	6	71
FM	15	0	**18**	0	1	34
OW	6	0	0	**52**	0	58
SH	5	5	0	0	**23**	33
Total	124	56	27	52	33	**292**

Table 8

Confusion matrix for high water Touzi polarimetric decomposition classification, high water season least accurate classification of Lago Grande de Curuai floodplain *várzea*. Land cover and vegetation classes are: EM — emergent macrophytes; FF — floodable forest; FM — floating macrophytes; OW — open water and SH — shrubs.

High water Touzi						
Classes	EM	FF	FM	OW	SH	Total
EM	**13**	4	2	1	8	28
FF	18	**47**	11	5	9	90
FM	0	0	**11**	3	0	14
OW	0	0	0	**118**	0	118
SH	18	5	3	0	**16**	42
Total	49	56	27	127	33	**292**

estimate using other real and/or angular descriptors, such as Entropy and Phase-difference. As C-band is strongly attenuated by dense vegetation canopies, scattering intensities are similar for plant types with subtle structural differences (Gosselin, Touzi and Cavayas, 2013) and for densely vegetated floodplains (Costa, 2004; Henderson & Lewis, 2008; Hess et al., 1990), hindering the ability of Cloude–Pottier α angle, Entropy and Anisotropy, and Touzi Phase-difference and α angle to detect subtle differences in backscattering mechanisms. The main, secondary and tertiary scattering mechanism types for each vegetation are similar and mainly differ in intensity, not in the nature of the scattering mechanism. Touzi Helicity and Orientation descriptors were of little use for discriminating *várzea* vegetation targets, as they were almost random. The low accuracy indexes obtained are strongly related to the wavelength and/or the similarity of the vegetation types, and the accuracy of Touzi and Cloude–Pottier based classifications can be higher when mapping less-similar wetland vegetation types (Millard & Richardson, 2013) and/or when using longer wavelengths (Sartori et al., 2011).

4.2. Dual-season classification

Wetland environments, and *várzeas* in particular, are very dynamic landscapes, and the backscattering of each vegetation type is strongly affected by hydrological variation. In general, all dual-season classifications yielded higher accuracies than single-season images and were able to discriminate forest, woody and grass patches with similar structures but different phenology and flooding durations. As their backscattering mechanism changes in both intensity and type between the high and low water seasons, the RF classifier was able to detect seasonal backscattering patterns and accurately map these classes.

For the woody classes (SH and FF), the main noticeable difference between HW and LW backscattering was related to changes in double-bounce occurrence. This type of scattering occurred with more intensity in the SH class, composed by shorter woody individuals with less dense and more fragmented canopies, and subject to longer flooding durations. These characteristics make SH canopies less attenuating to the C-band signal and allow the microwaves to penetrate canopy gaps and thus interact more intensely with the flooding, increasing

double-bounce occurrence. Conversely, double-bounce occurrence is less intense for the FF class, composed by taller trees with denser canopies and found on the highest elevations within the *várzea*, thus having floods with shorter durations and heights.

Double-bounce scattering in herbaceous/grasses targets had similar intensities to woody classes, and in single-season classifications, there was a large overlap in backscattering from all floodable vegetation classes. During the low water season, double-bounces may still occur in areas that are flooded for longer periods or are quasi-permanent flooded, such as areas of *Montrichardia spp.* occurrence. This behavior may explain part of the confusion between EM and SH classes, as these classes have longer flooding periods and therefore similar temporal backscattering signatures. Volumetric scattering intensity for herbaceous plants/grasses, comprised mainly by the EM class, is also similar to those observed in woody vegetation, but seasonal changes were more detectable due their annual growth cycle.

Several studies highlight the importance of dual- and multi-seasonal remote sensing data for land cover classification of *várzea* and other wetlands (Costa, 2004; Kwoun & Lu, 2009; Marti-Cardona et al., 2010; Silva et al., 2010). Several of these studies analyze the temporal backscattering signatures of plant communities and/or other targets without attempting classification (Cable, Kovacs, Shang, & Jiao, 2014; Koch, Schmid, Reyes, & Gumuzzio, 2012). Other studies use dual- or multiseasonal information to obtain a single best classification, but there is little discussion about the impacts of seasonality and the selected dates used in classification accuracy (Evans & Costa, 2013). Few studies truly investigate and discuss the impacts of date choice on classification accuracy, or attempt to identify optimum date combinations (Hess et al., 2003; Jiao et al., 2014). Our study thus contributes by quantifying the impacts of both (1) seasonality and (2) polarimetric information on classification accuracy, when combined or not, reinforcing the results of previous studies on dual- or multi-seasonal SAR/ PolSAR wetland mapping.

5. Conclusion

Our results show that single-season full-polarimetric SAR can achieve classification accuracies that are similar or, in some cases,

Table 7

Confusion matrix for dual-season Touzi polarimetric decomposition classification, dual-season least accurate classification of Lago Grande de Curuai floodplain *várzea*. Land cover and vegetation classes are: EM — emergent macrophytes; FF — floodable forest; FM — floating macrophytes; OW — open water, SH — shrubs and VF — *várzea* fields.

Dual-season Touzi							
Classes	EM	FF	FM	OW	SH	VF	Total
EM	**14**	6	2	0	2	0	24
FF	16	**45**	4	0	7	0	72
FM	5	1	**21**	1	1	9	38
OW	0	0	0	**42**	0	2	44
SH	14	4	0	0	**23**	1	42
VF	0	0	0	9	0	**63**	72
Total	49	56	27	52	33	75	**292**

Table 9

Confusion matrix for low water Touzi polarimetric decomposition classification, low water season lest accurate classification of Lago Grande de Curuai floodplain *várzea*. Land cover and vegetation classes are: EM — emergent macrophytes; FF — floodable forest; FM — floating macrophytes; OW — open water and SH — shrubs.

Low water Touzi						
Classes	EM	FF	FM	OW	SH	Total
EM	**71**	14	10	3	6	104
FF	27	**36**	3	0	8	74
FM	12	0	**13**	0	1	26
OW	4	0	1	**46**	0	51
SH	10	6	0	3	**18**	37
Total	124	56	27	52	33	**292**

higher to those achievable by dual-season dual-pol SAR classifications, especially during the high water season ($\kappa = 0.7$–0.8; AD $= 3$–5% and QD $= 10$–15%). Therefore, the use of PolSAR images may reduce the need for multiple season imagery, reducing overall acquisition costs and enabling detailed assessment of vegetation cover at any chosen period of the hydrological cycle.

Still, *várzea* plant communities are very similar in terms of structure and phenology, and dual-seasonal PolSAR data was capable of achieving the highest classification accuracies for all classes, combining the better structural discrimination achieved by PolSAR with the hydrological and phenological information brought by dual-season data. Model-based decompositions and, to a lesser degree, the linear polarizations present in the C-matrix stood as the most accurate polarimetric descriptors for discriminating land cover and vegetation classes in *várzea* floodplains, for both single and dual-season images.

PolSAR data in all main SAR wavelengths (C, X and L bands) are readily available for commercial and scientific uses, and our results can help guide data acquisition strategies by research institutions, government agencies and the private sector. We were able to achieve very accurate classifications in this study ($\kappa > 0.8$, AD $< 3\%$ and QD $< 10\%$), showing that operational uses of PolSAR data for wetland mapping are a reality. The methods described in this study can be applied to generate accurate vegetation maps, contributing to improve habitat distribution, biomass and productivity, and greenhouse gas emission estimates, for both herbaceous and forest vegetation, contributing to the understanding of climate and land cover change impacts in the Amazon *várzea* and similar wetlands.

Acknowledgments

Appendix A. Supplementary data

Supplementary data to this article can be found online at http://dx.doi.org/10.1016/j.rse.2015.12.013.

References

Ainsworth, T. L., Kelly, J. P., & Lee, J. S. (2009). Classification comparisons between dual-pol, compact polarimetric and quad-pol SAR imagery. *ISPRS Journal of Photogrammetry and Remote Sensing*, 64(5), 464–471. http://dx.doi.org/10.1016/j.isprsjprs.2008.12.008.

Arantes, C. C., Castello, L., Cetra, M., & Schilling, A. (2013). Environmental influences on the distribution of arapaima in Amazon floodplains. *Environmental Biology of Fishes*, 96(10–11), 1257–1267. http://dx.doi.org/10.1007/s10641-011-9917-9.

Arnesen, A. S., Silva, T. S. F., Hess, L. L., Novo, E. M. L. M., Rudorff, C. M., Chapman, B. D., & McDonald, K. C. (2013). Monitoring flood extent in the lower Amazon River floodplain using ALOS/PALSAR ScanSAR images. *Remote Sensing of Environment*, 130, 51–61. http://dx.doi.org/10.1016/j.rse.2012.10.035.

Arraut, E. M., Marmontel, M., Mantovani, J. E., Novo, E. M. L. M., Macdonald, D. W., & Kenward, R. E. (2010). The lesser of two evils: Seasonal migrations of Amazonian manatees in the Western Amazon. *Journal of Zoology*, 280(3), 247–256. http://dx.doi.org/10.1111/j.1469-7998.2009.00655.x.

Barrett, B., Nitze, I., Green, S., & Cawkwell, F. (2014). Assessment of multi-temporal, multi-sensor radar and ancillary spatial data for grasslands monitoring in Ireland using machine learning approaches. *Remote Sensing of Environment*, 152(529), 109–124. http://dx.doi.org/10.1016/j.rse.2014.05.018.

Bhang, K. J., Schwartz, F. W., & Braun, A. (2007). Verification of the vertical error in C-band SRTM DEM using ICESat and Landsat-7, Otter Tail County, MN. *IEEE Transactions on Geoscience and Remote Sensing*, 45(1), 36–44.

Breiman, L. (2001). Random forests. *European Journal of Mathematics*, 45(1), 5–32.

Brisco, B., Kapfer, M., Hirose, T., Tedford, B., & Liu, J. (2011). Evaluation of C-band polarization diversity and polarimetry for wetland mapping. *Canadian Journal of Remote Sensing*, 37(1), 82–92. http://dx.doi.org/10.5589/m11-017.

Brisco, B., Li, K., Tedford, B., Charbonneau, F., Yun, S., & Murnaghan, K. (2013). Compact polarimetry assessment for rice and wetland mapping. *International Journal of Remote Sensing*, 34(6), 1949–1964. http://dx.doi.org/10.1080/01431161.2012.730156.

Cable, J. W., Kovacs, J. M., Shang, J., & Jiao, X. (2014). Multi-temporal polarimetric RADARSAT-2 for land cover monitoring in northeastern Ontario, Canada. *Remote Sensing*, 6(3), 2372–2392. http://dx.doi.org/10.3390/rs6032372.

Castello, L., Mcgrath, D. G., Hess, L. L., Coe, M. T., Lefebvre, P. A., Petry, P., ... Arantes, C. C. (2013). The vulnerability of Amazon freshwater ecosystems. *Conservation Letters*, 6(4), 217–229. http://dx.doi.org/10.1111/conl.12008.

Cloude, S. R., & Pottier, E. (1996). A review of target decomposition theorems in radar polarimetry. *IEEE Transactions on Geoscience and Remote Sensing*, 34(2), 498–518.

Congalton, R. G. (1991). A review of assessing the accuracy of classifications of remotely sensed data. *Remote Sensing of Environment*, 37(1), 35–46. http://dx.doi.org/10.1016/0034-4257(91)90048-B.

Core Team, R. (2014). *R: A language and environment for statistical computing*. Vienna, Austria: R Foundation for Statistical Computing (Retrieved from http://r-project.org).

Costa, M. P. F. (2004). Use of SAR satellites for mapping zonation of vegetation communities in the Amazon floodplain. *International Journal of Remote Sensing*, 25(10), 1817–1835. http://dx.doi.org/10.1080/0143116031000116985.

Costa, M. P. F., Niemann, O., Novo, E., & Ahern, F. (2002). Biophysical properties and mapping of aquatic vegetation during the hydrological cycle of the Amazon floodplain using JERS-1 and Radarsat. *International Journal of Remote Sensing*, 23(7), 1401–1426. http://dx.doi.org/10.1080/01431160110092957.

Engdahl, M., Minchella, A., Marinkovic, P., Veci, L., & Lu, J. (2012). NEST: An esa open source toolbox for scientific exploitation of SAR data. *International Geoscience and Remote Sensing Symposium (IGARSS)*, Vol. 1. (pp. 5322–5324). http://dx.doi.org/10.1109/IGARSS.2012.6352406.

Evans, T. L., & Costa, M. (2013). Landcover classification of the Lower Nhecol??ndia subregion of the Brazilian Pantanal Wetlands using ALOS/PALSAR, RADARSAT-2 and ENVISAT/ASAR imagery. *Remote Sensing of Environment*, 128, 118–137. http://dx.doi.org/10.1016/j.rse.2012.09.022.

Ferreira-Ferreira, J., Silva, T. S. F., Streher, A. S., Affonso, A. G., Furtado, L. F., de A. Forsberg, B. R., & Novo, E. M. L. M. (2014). Combining ALOS/PALSAR derived vegetation structure and inundation patterns to characterize major vegetation types in the Mamirauá Sustainable Development Reserve, Central Amazon floodplain, Brazil. *Wetlands Ecology and Management*. http://dx.doi.org/10.1007/s11273-014-9359-1.

Freeman, A., & Durden, S. L. (1998). A three-component scattering model for polarimetric SAR data. *IEEE Transactions on Geoscience and Remote Sensing*, 36(3), 963–973. http://dx.doi.org/10.1109/36.673687.

Furtado, L. F., Silva, de A., Fernandes, T. S. F., Novo, P. J. F., & de M., E. M. L. (2015). Land cover classification of Lago Grande de Curuai (Amazon, Brazil) using multi-sensor and image fusion techniques. *Acta Amazonica*, 45(2), 195–202. http://dx.doi.org/10.1590/1809- 4392201401439.

Garcia, C. E., Roberto, J., Mura, J. C., Johann, H., & Kux, H. (2012). Análise do potencial de imagem TerraSAR-X para mapeamento temático no sudoeste da Amazônia brasileira. *Acta Amazonica*, 42(2), 205–214.

Gosselin, G., Touzi, R., & Cavayas, F. (2013). Polarimetric Radarsat-2 wetland classification using the Touzi decomposition: case of the Lac Saint-Pierre Ramsar wetland. *Canadian Journal of Remote Sensing*, 39(6), 491–506. http://dx.doi.org/10.5589/m14-002.

Henderson, F. M., & Lewis, A. J. (2008). Radar detection of wetland ecosystems: A review. *International Journal of Remote Sensing*, 29(20), 5809–5835. http://dx.doi.org/10.1080/01431160801958405.

Hess, L. L., Melack, J. M., Novo, E. M. L. M., Barbosa, C. C. F., & Gastil, M. (2003). Dual-season mapping of wetland inundation and vegetation for the central Amazon Basin. *Remote Sensing of Environment*, 87(4), 404–428. http://dx.doi.org/10.1016/j.rse.2003.04.001.

Hess, L. L., Melack, J. M., & Simonett, D. S. (1990). Radar detection of flooding beneath the forest canopy — A review. *International Journal of Remote Sensing*, 11(7), 1313–1325.

Hess, L. L., Melack, J. M., Filoso, S., & Yong, Wang (1995). Delineation of inundated area and vegetation along the Amazon floodplain with the SIR-C synthetic aperture radar. *IEEE Transactions on Geoscience and Remote Sensing*, 33(4), 896–904. http://dx.doi.org/10.1109/36.406675.

Hess, Laura L., Melack, John M., Affonso, Adriana G., Barbosa, Claudio, Gastil-Buhl, Mary, & M. L. M, Novo, Evlyn (2015). Wetlands of the Lowland Amazon Basin: Extent. *VegetativeCover, and Dual-season Inundated Area as Mapped with JERS-1 Synthetic ApertureRadar. Wetlands*, 35(4), 745–756.

Jiao, X., Kovacs, J. M., Shang, J., McNairn, H., Walters, D., Ma, B., & Geng, X. (2014). Object-oriented crop mapping and monitoring using multi-temporal polarimetric RADARSAT-2 data. *ISPRS Journal of Photogrammetry and Remote Sensing*, 96, 38–46. http://dx.doi.org/10.1016/j.isprsjprs.2014.06.014.

Jarvis, A., Reuter, H. I., & Nelson, A. (2008). Hole-filled SRTM for the globe version 4. available from the CGIAR-CSI SRTM 90 m Database http://srtm.csi.cgiar.org

Junk, W. J. (1997). *The Central Amazon floodplain — Ecology of a pulsing system*. Verlag: Springer (548 pp.).

Junk, W. J., Bayley, P. B., & Sparks, R. E. (1989). The flood pulse concept in river–floodplain systems. *Canadian Special Publication of Fisheries and Aquatic Sciences*, 106(1), 110–127. http://dx.doi.org/10.1371/journal.pone.0028909.

Junk, W. J., Piedade, M. T. F., Schöngart, J., & Wittmann, F. (2012). A classification of major natural habitats of Amazonian white-water river floodplains (*várzeas*). *Wetlands*

Ecology and Management, 20(6), 461–475. http://dx.doi.org/10.1007/s11273-012-9268-0.

Kasischke, E. S., Melack, J. M., & Dobson, M. C. (1997). The use of imaging radars for ecological applications − A review. *Remote Sensing of Environment*, 59(2), 141–156. http://dx.doi.org/10.1016/S0034-4257(96)00148-4.

Koch, M., Schmid, T., Reyes, M., & Gumuzzio, J. (2012). Evaluating full polarimetric C- and L-band data for mapping wetland conditions in a semi-arid environment in central Spain. *IEEE Journal of Selected Topics in Applied Earth Observations and Remote Sensing*, 5(3), 1033–1044. http://dx.doi.org/10.1109/JSTARS.2012.2202091.

Kwoun, O. -I., & Lu, Z. (2009). Multi-temporal RADARSAT-1 and ERS backscattering signatures of coastal wetlands in southeastern Louisiana. *Photogrammetric Engineering and Remote Sensing*, 75(5), 607–615 (Retrieved from http://www.asprs.org/publications/pers/2009journal/may/abstracts.html#607).

Lang, M. W., Townsend, P. a., & Kasischke, E. S. (2008). Influence of incidence angle on detecting flooded forests using C-HH synthetic aperture radar data. *Remote Sensing of Environment*, 112(10), 3898–3907. http://dx.doi.org/10.1016/j.rse.2008.06.013.

Lee, J. S., & Pottier, E. (2009). *Polarimetric radar imaging: From basics to applications.* Boca Raton: CRC Press (440 pp.).

Lee, J. S., Grunes, M. R., & Pottier, E. (2001). Quantitative comparison of classification capability: Fully polarimetric versus dual and single-polarization SAR. *IEEE Transactions on Geoscience and Remote Sensing*, 39(11), 2343–2351. http://dx.doi.org/10.1109/36.964970.

Liaw, A., & Wiener, M. (2002). Classification and regression by randomForest. *R News*, 2(3), 18–22.

Marti-Cardona, B., Lopez-Martinez, C., Dolz-Ripolles, J., & Bladè-Castellet, E. (2010l). ASAR polarimetric, multi-incidence angle and multitemporal characterization of Doñana wetlands for flood extent monitoring. *Remote Sensing of Environment*, 114(11), 2802–2815. http://dx.doi.org/10.1016/j.rse.2010.06.015.

Martinez, J. M., & Le Toan, T. (2007). Mapping of flood dynamics and spatial distribution of vegetation in the Amazon floodplain using multitemporal SAR data. *Remote Sensing of Environment*, 108(3), 209–223. http://dx.doi.org/10.1016/j.rse.2006.11.012.

Melack, J. M., & Hess, L. L. (2010). Remote sensing of the distribution and extent of wetlands in the Amazon Basin. In W. J. Junk, M. T. F. Piedade, F. Wittmann, J. Schöngart, & P. Parolin (Eds.), *Amazonian floodplain forests: Ecophysiology, biodiversity and sustainable management* (pp. 43–59). Springer. http://dx.doi.org/10.1007/978-90-481-8725-6.

Millard, K., & Richardson, M. (2013). Wetland mapping with LiDAR derivatives, SAR polarimetric decompositions, and LiDAR-SAR fusion using a random forest classifier. *Canadian Journal of Remote Sensing*, 39(4), 290–307. http://dx.doi.org/10.5589/m13-038.

Pontius, R. G., & Millones, M. (2011). Death to Kappa: Birth of quantity disagreement and allocation disagreement for accuracy assessment. *International Journal of Remote Sensing*, 32(15), 4407–4429. http://dx.doi.org/10.1080/01431161.2011.552923.

Pottier, E., Ferro-Famil, L., Allain, S., Cloude, S., Hajnsek, I., Papathanassiou, K., ... Desnos, Y. L. (2009i). Overview of the PolSARpro v4.0 Software. The open source toolbox for polarimetric and interferometric polarimetric SAR data processing. *International Geoscience and Remote Sensing Symposium (IGARSS)*, Vol. 4. (pp. 936–939). http://dx.doi.org/10.1109/IGARSS.2009.5417532.

Qi, Z., Yeh, A. G. -O., Li, X., & Lin, Z. (2012). A novel algorithm for land use and land cover classification using RADARSAT-2 polarimetric SAR data. *Remote Sensing of Environment*, 118, 21–39. http://dx.doi.org/10.1016/j.rse.2011.11.001.

Renó, V. F., Novo, E. M. L. M., Almeida-Filho, R., & Suemitsu, C. (2011a). Mapeamento da antiga cobertura vegetal de *várzea* do Baixo Amazonas a partir de imagens históricas (1975–1981) do Sensor MSS-Landsat. *Acta Amazonica*, 41(1), 47–56. http://dx.doi.org/10.1590/S0044-59672011000100006.

Renó, V. F., Novo, E. M. L. M., Suemitsu, C., Rennó, C. D., & Silva, T. S. F. (2011b). Assessment of deforestation in the lower Amazon floodplain using historical Landsat MSS/TM imagery. *Remote Sensing of Environment*, 115(12), 3446–3456. http://dx.doi.org/10.1016/j.rse.2011.08.008.

Rudorff, C. M., Melack, J. M., & Bates, P. D. (2014). Flooding dynamics on the lower Amazon floodplain: 1. Hydraulic controls on water elevation, inundation extent, and river–floodplain discharge. *Water Resources Research*, 50(1), 619–634. http://dx.doi.org/10.1002/2013WR014091.

Sartori, L. R., Imai, N. N., Mura, J. C., Novo, E. M. L. D. M., & Silva, T. S. F. (2011). Mapping macrophyte species in the amazon floodplain wetlands using fully polarimetric ALOS/PALSAR data. *IEEE Transactions on Geoscience and Remote Sensing*, 49(12 PART 1), 4717–4728. http://dx.doi.org/10.1109/TGRS.2011.2157972.

Silva, T. S. F., Costa, M. P. F., & Melack, J. M. (2010). Spatial and temporal variability of macrophyte cover and productivity in the eastern Amazon floodplain: A remote sensing approach. *Remote Sensing of Environment*, 114(9), 1998–2010. http://dx.doi.org/10.1016/j.rse.2010.04.007.

Silva, T. S. F., Costa, M. P. F., Melack, J. M., & Novo, E. M. L. M. (2008). Remote sensing of aquatic vegetation: Theory and applications. *Environmental Monitoring and Assessment*, 140(1–3), 131–145. http://dx.doi.org/10.1007/s10661-007-9855-3.

Silva, T. S. F., Melack, J. M., Streher, A. S., Ferreira-Ferreira, J., & de A. Furtado, L. F. (2015,). Capturing the dynamics of Amazonian wetlands using synthetic aperture radar: Lessons learned and future directions. In R. Tiner, M. Lang, & V. Klemas (Eds.), *Remote sensing of wetlands: Applications and advances* (pp. 453–470). Boca Raton, Florida: CRC Press. http://dx.doi.org/10.1201/b18210-25.

Touzi, R. (2007). Target scattering decomposition in terms of roll-invariant target parameters. *IEEE Transactions on Geoscience and Remote Sensing*, 45(1), 73–84. http://dx.doi.org/10.1109/TGRS.2006.886176.

USGS (2009). *Global land survey, 2000, Landsat TM, 30 m scene LT52280612009280CUB01.* Sioux Falls, South Dakota: USGS.

Van Beijma, S., Comber, A., & Lamb, A. (2014). Random forest classification of salt marsh vegetation habitats using quad-polarimetric airborne SAR, elevation and optical RS data. *Remote Sensing of Environment*, 149, 118–129. http://dx.doi.org/10.1016/j.rse.2014.04.010.

Van Zyl, J. J. (1992). Application of Cloude's target decomposition theorem to polarimetric imaging radar data. *Radar polarimetry, SPIE-1748* (pp. 184–212).

Wittmann, F., Junk, W. J., & Piedade, M. T. F. (2004). The *várzea* forests in Amazonia: Flooding and the highly dynamic geomorphology interact with natural forest succession. *Forest Ecology and Management*, 196(2–3), 199–212. http://dx.doi.org/10.1016/j.foreco.2004.02.060.

Wittmann, F., Schöngart, J., & Junk, W. J. (2010). Phytogeography, species diversity, commynity structure and dynamics of central Amazonian floodplain forests. In W. J. Junk, M. T. F. Piedade, F. Wittmann, J. Schöngart, & P. Parolin (Eds.), *Amazonian floodplain forests: Ecophysiology, biodiversity and sustainable management* (pp. 61–102). Springer. http://dx.doi.org/10.1007/978-90-481-8725-6.

Yamaguchi, Y., Yajima, Y., & Yamada, H. (2006). A four-component decomposition of POLSAR images based on the coherency matrix. *IEEE Geoscience and Remote Sensing Letters*, 3(3), 292–296. http://dx.doi.org/10.1109/LGRS.2006.869986.